JGR Oceans

RESEARCH ARTICLE
10.1029/2018JC014607

# Sea State Trends and Variability: Consistency Between Models, Altimeters, Buoys, and Seismic Data (1979–2016)

**Justin E. Stopa**[1,2], **Fabrice Ardhuin**[2], **Eleonore Stutzmann**[3], **and Thomas Lecocq**[4]

[1]Department of Ocean Resources and Engineering, School of Ocean and Earth Science and Technology, University of Hawaii at Manoa, Honolulu, HI, USA, [2]University Brest, CNRS, IRD, Ifremer, Laboratoire d'Océanographie Physique et Spatiale (LOPS), IUEM, Brest, France, [3]Institut de Physique du Globe de Paris, Paris, France, [4]Seismology-Gravimetry, Royal Observatory of Belgium, Brussels, Belgium

**Key Points:**
- Reanalysis products are not consistent in time due to changes in assimilated satellite data sets
- Reanalysis winds speeds are corrected using wave height model-altimeter residuals
- Closer agreement of trends between altimeter, hindcast, seismic, and buoy data sets is reached

**Correspondence to:**
J. E. Stopa,
stopa@hawaii.edu

**Citation:**
Stopa, J. E., Ardhuin, F., Stutzmann, E., & Lecocq, T. (2019). Sea state trends and variability: Consistency between models, altimeters, buoys, and seismic data (1979–2016). *Journal of Geophysical Research: Oceans*, *124*, 3923–3940. https://doi.org/10.1029/2018JC014607

Received 26 SEP 2018
Accepted 12 APR 2019
Accepted article online 22 APR 2019
Published online 20 JUN 2019

**Abstract** Wave hindcasts of long time series (>30 years) have been instrumental in understanding the wave climate. However, it is still difficult to have a consistent reanalysis suitable for study of trends and interannual variability. Here we explore the consistency of a wave hindcast with independent observations from moored buoys, satellite altimeters, and seismic data. We use the Climate Forecast System Reanalysis (CFSR) winds to drive a wave model since extreme events are generally well captured. Unfortunately, the original CFSR winds are not homogeneous in time. We systematically modify this wind field in time and space to produce a wave field that has homogeneous differences against the Globwave/SeaStateCCI altimeter wave height database. These corrections to the winds and resulting waves are validated using independent buoy and microseism data. We particularly use seismic data in the dominant double-frequency band, around 5-s period, that are generated by opposing waves of equal frequencies. The seismic data confirms that our correction of time-varying biases is consistent, even in remote and undersampled region such as the Southern Ocean where the original CFSR biases are strongest. Our analysis is performed on monthly time series, and we expect the monthly statistics to be better suited for climate studies. Remaining issues with time consistency of reanalysis products and associated wave hindcasts are further discussed.

## 1. Introduction

The sea state is an Essential Climate Variable with important applications in ocean and coastal engineering as well as effects on the climate system (e.g., Cavaleri et al., 2012). Wave hindcasts and reanalysis products have improved our understanding of the climate for the past several decades, which includes high sea states and interannual variability (Fan et al., 2012; Reguero et al., 2012; Wang & Swail, 2001). Typically, wave hindcasts are generated from reanalysis data sets of winds, because they are evenly spaced in time and space and have high spatial resolution. To date there are many different forcing wind fields available that can be used to drive a wave hindcast (Stopa, 2018). Some of the reanalysis systems also include an ocean wave component, like the European Center for Medium-Range Weather Forecasts (ECMWF) Reanalysis Interim (ERAI) that assimilate altimeter significant wave heights into the product, starting in 1992. This makes it very difficult to estimate a meaningful trend combining years before and after 1992 (Aarnes et al., 2015; Dee et al., 2011). ERAI winds seem to be more consistent in time, compared to the National Centers for Environmental Prediction (NCEP) Climate Forecast System Reanalysis (CFSR), but they underestimate the largest events (Stopa & Cheung, 2014b). Recently, ECMWF released an updated reanalysis called their 5th generation (ERA5) which has model improvements and higher time and space resolution relative to ERAI (for Medium-Range Weather Forecasts, E. C., 2017). The time inconsistencies prompted some to correct wave hindcasts using statistical techniques such as Caires and Sterl (2005) and Reguero et al. (2012). In any case, it is fundamentally difficult to overcome the inconsistencies of reanalysis data sets due to the changing quantity and quality of the satellite data incorporated into the products (see Figure 10 of Dee et al., 2011). Therefore, wave hindcasts still need improvements to be consistent in time while resolving extremes. The lack of a homogeneous wave hindcast is a clear limit to our understanding of the wave climate.

Wave reanalyses that assimilate all satellite observations are difficult to evaluate with independent data. Satellite altimeters measure the significant wave heights ($H_s$) and sea surface roughness. The near-surface

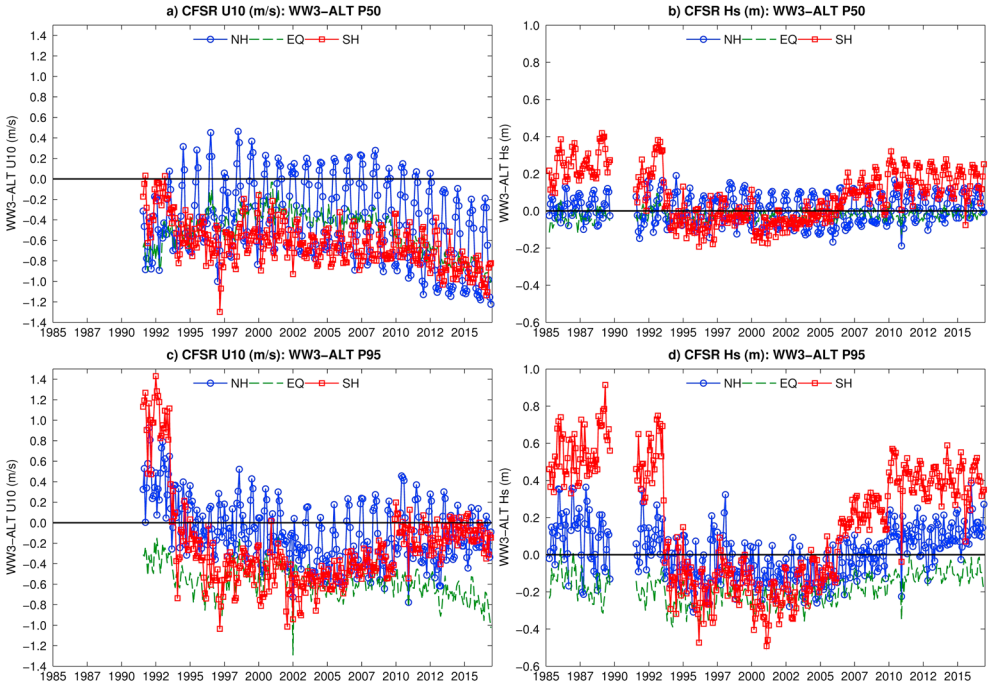


**Figure 1.** Monthly residuals: difference between CFSR reanalysis and altimeter wind speeds (a and c); difference between wave hindcast using CFSR versus altimeter significant wave heights (b and d). Panels (a) and (b) represent the median (P50), and panels (c) and (d) are the 95th percentile (P95). Latitudinal bands are denoted as Northern Hemisphere (NH: 30–60°N), equatorial region (EQ: 30°S to 30°N), and the Southern Hemisphere (SH: 30–60°S). CFSR = Climate Forecast System Reanalysis.

wind speeds at 10 m ($U_{10}$) can be estimated from the sea surface roughness (Gourrion et al., 2002). This altimeter-derived wind speeds have never been assimilated. Therefore, comparing $U_{10}$ and $H_s$ from the altimeters to a reanalysis data set and a wave hindcast offers a means to assess the products independently and at a global scale. With the exception of ECMWF reanalyzes (e.g., ERAI and ERA5), the measured $H_s$ is also an independent measurement.

To illustrate some of the errors associated with CFSR winds used in a wave hindcast, we show in Figure 1 monthly differences between measured $U_{10}$ and $H_s$ and the GlobWAVE/SeaStateCCI altimeter database (Queffeulou, 2013; Sepulveda et al., 2015). It is clear that the $U_{10}$ and $H_s$ at the 50th and 95th percentiles (P50 and P95) are higher before 1993, as discussed by Chawla et al. (2013) and Rascle and Ardhuin (2013). There are several other notable features such as the difference between the Northern and Southern Hemispheres and the increasing trend from 2005 to 2010. The details of these plots will be discussed throughout the manuscript. Here, we want to demonstrate the value in further analyzing the consistency of a wave hindcast relative to independent data sources.

Specifically, in this work we analyze the time consistency of a wave hindcast forced by CFSR using data from altimeters, moored buoys, and seismic stations. We particularly use seismic data in the dominant double-frequency band, around 5-s period, that are generated by opposing waves of equal frequencies (Ardhuin et al., 2011; Hasselmann, 1963; Kedar et al., 2007; Longuet-Higgins, 1950). These signals are very sensitive to wave height changes and have been used to estimate wave heights (Ardhuin et al., 2012; Bromirski et al., 1999; Zopf et al., 1976). We choose to use CFSR to drive the wave hindcast because the time and spatial resolution is the highest (1 hr and 20–40 km) and reasonably captures the extremes (Hemer et al., 2017; Perez et al., 2017; Stopa & Cheung, 2014b; Stopa, 2018). Since the altimeter database is relatively long (1985–1989, 1992–2016) and covers the global ocean we heavily rely on these reference data.

The goal of our study is twofold. The first objective is to improve the time consistency of a wave hindcast driven by CFSR. Our analysis is performed on monthly basis in order to have enough data to sufficiently capture statistical properties. Taking the merged altimeter $H_s$ as a reference, we systematically modify the CFSR wind field to produce a homogeneous wave field. This leaves us with the moored buoy and seismic

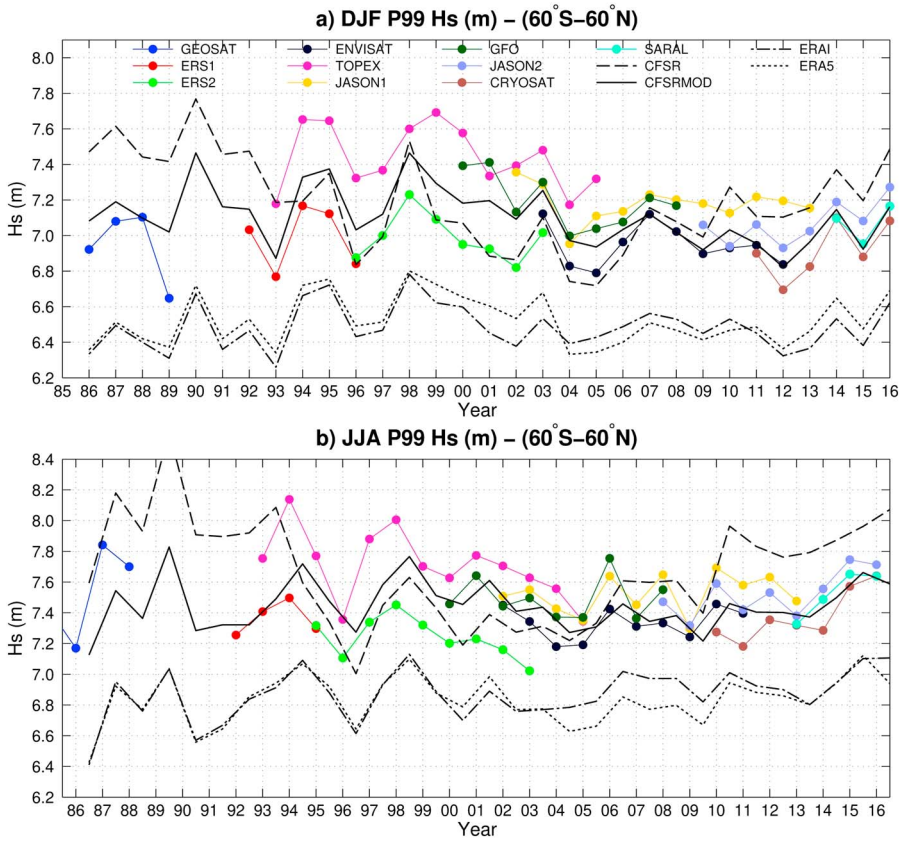


**Figure 2.** Merged altimeter $H_s$ database where panel (a) shows December-January-February (DJF) $H_s$ P99 and (b) shows June-July-August (JJA) globally (60°S to 60°N). The colors denote the altimeter platform and the black lines without markers represent the wave hindcasts from this study: CFSR and CFSRMOD and European Center for Medium-Range Weather Forecasts products: European Center for Medium-Range Weather Forecasts Reanalysis Interim and ERA5. CFSR = Climate Forecast System Reanalysis.

observations to further assess the correction and homogeneity of the hindcast. The second objective is to work toward a consistent estimation of trends, discussing the inhomogeneities in wave climate records from the various data sources: (1) wave hindcasts, (2) altimeters, (3) moored buoys, and (4) seismic stations. When discussing trends of approximately 0.5–2 cm/year as quantified by Young et al. (2011), various factors such as the assimilation method and the amount and quality of satellite data being assimilated into the reanalysis are important.

The manuscript will proceed as follows. In section 2, we describe the data sets and model setup. Next in section 3, we present our proposed correction which is based on altimeter $H_s$. In section 4, we compare our modified wave hindcast with independent data from buoys and seismic stations. Our discussions and conclusions follow in sections 5 and 6, respectively.

## 2. Data Sets and Model Setup

### 2.1. Data Sets

#### 2.1.1. NCEP CFSR

The NCEP CFSR is a global coupled system composed of atmosphere, ocean, land, and ice models (Saha et al., 2010). The reanalysis data set begins with the modern satellite era in 1979 and extends to present day. Version 1 from 1979–2010 has spatial resolution of 38 km in the atmospheric model and uses assimilation in 3-dimensions with initialization every 6 hr and hourly forecasts. Version 2 has spatial resolution of 22 km in the atmospheric model and begins in 2011 (Saha et al., 2014). Version 2 has improved performance in tropical regions. CFSR has a dynamic sea ice model and the sea ice concentrations are used as input into the wave model. CFSR has been used to generate many wave hindcasts, including those by Chawla et al. (2013), Rascle and Ardhuin (2013), and Perez et al. (2017), which successfully capture important characteristics of the wave field such as Stokes drift, and mean square slope, and climate variability (Stopa et al., 2016).

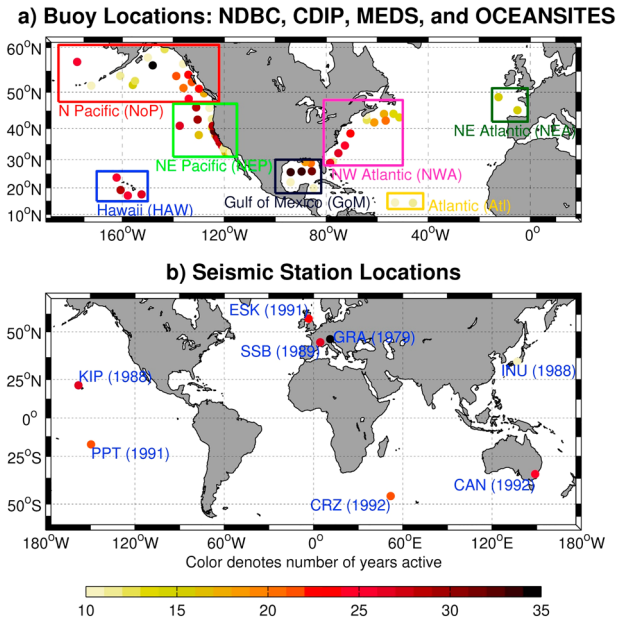


**Figure 3.** Buoy and seismic station locations: Panel (a) shows the buoy location with the color representing the number of years active and grouped in various regions. Each buoy time series spans at least 10 years from the NDBC, CDIP, MEDS, and Oceansites networks. Panel (b) shows the seismic station locations with the color represents the number of years active and the starting year in parentheses. NDBC = National Data Buoy Center; CDIP = Coastal Data Information Program; MEDS = Marine Environmental Data Service.

### 2.1.2. Merged Altimeter Database

The multiplatform altimeter product (abbreviated ALT herein) was quality controlled and calibrated by Queffeulou and Croize-Fillon (2017). It was produced as part of the GlobWAVE project and is now extended to form the first version of the Sea State Climate Change initiative database (SeaStateCCI). The data set spans 30 years from 1985 through 2016. The database includes the following 10 missions: GEOSAT (1985–1989), ERS1 (1991–1996), TOPEX (1993–2005), ERS2 (1996–2011), GFO (2000–2007), JASON1 (2002–2013), ENVISAT (2002–2012), JASON2 (2009–2016), CRYOSAT (2011–2016), and SARAL (2014–2016). Each mission is quality controlled and calibrated to moored buoys and cross calibrated between platforms. Note this data set includes both $U_{10}$ and a calibrated $H_s$ using 1-Hz data. The $U_{10}$ from GEOSAT is unreliable as noted by Zieger et al. (2009) and was not used in our analysis. This is the reason it was not included in Figure 1.

The sea state altimetry data set is reasonably consistent in time with small interplatforms deviations (see Figure 2). A recent study shows the consistency between platforms especially when the different missions are cross calibrated (Young et al., 2017). The deviations in Figure 2 are within 2–8% for monthly statistics at the 99th percentile (P99) and even smaller for average sea states (P50) at 1–3%. For example, in June-July-August 1994, the difference in the $H_s$ between TOPEX and ERS1 is 0.65 m, which is approximately 8% deviation between the platforms. Each platform is also observing the ocean differently because of their trajectories so some variations especially at P95 are expected. The largest deviations occur in the early part of the data record (1992–1998) when three altimeters are active (ERS1, TOPEX, and ERS2). The altimeter $H_s$ deviations between platforms will not change the outcome of this work since we typically take a regional average over a large scale and combine data from all missions together as a single merged product. However, improvements to the data set can be made and this is the focus of the ESA SeaStateCCI project.

For reference we plot the hindcast results for from this study including the original CFSR hindcast and after the wind speeds are modified (CFSRMOD). In addition, we included ERAI and ERA5 since these products assimilate the altimeter $H_s$ data. Aarnes et al. (2015) show that the analysis product of ERAI does not capture the trends as well as the 24- and 48-hr forecast products. Their results also suggest that the satellite altimetry introduces spurious $H_s$ trends into ERAI. These subtle effects are not seen in Figure 2. The homogeneity of ERAI and ERA5 in Figure 2 is expected to be due to a better treatment of other assimilated fields namely the large amount of scatterometer and radiometer winds (Dee et al., 2011). The CFSR products fall within

the range of altimeter observations, while the ECMWF products underestimate $H_s$ consistent with others (Rascle & Ardhuin, 2013; Stopa & Cheung, 2014a; Stopa et al., 2016).

#### 2.1.3. Buoys

Several buoy networks that have open data archives covering 30 years or more. In this study, we use data from the National Data Buoy Center (NDBC), Coastal Data Information Program (CDIP), Marine Environmental Data Service (MEDS), and the collaborative project Oceansites. Because our focus is to produce a global-scale wave hindcast with approximate spatial resolution of 50 km, we only use buoys located in deep water (>200 m), sufficiently far from coastlines (>30 km), and exposed to open ocean conditions (e.g., not sheltered by an offshore island). With these constraints the wave model should not be affected by wave transformation that are not well captured at these course spatial scales and have reasonable quality at the buoy locations. Figure 3a shows the locations of the buoys, which are limited to the Northern Hemisphere. The NDBC network is the most extensive network. We note that buoys in the Northwest Atlantic (WMO41001, WMO41002, WMO41006, and WMO44004), Gulf of Mexico (WMO42001, WMO42002, and WMO42003), North Pacific (WMO46003 and WMO46035), Northeast Pacific (WMO46002, WMO46006, WMO46005, WMO46006, WMO46011, WMO46014, WMO46022, WMO46023, WMO46025, and WMO46028), and Hawaii (WMO51001, WMO51002, WMO51002, and WMO51004) measured waves for several years in the 1980s. These long records are important to check the consistency of the hindcast at the time when the CFSR reanalysis is much less constrained by assimilated atmospheric data (Saha et al., 2010). We grouped the buoys into regions based on their geographic location since they have similar climates. We interpolate the model data in time and space to match the buoy observations. The buoy time series are quality controlled, but sensors, hulls, and processing units change over these many years (Gemmrich et al., 2011). These changes presumably affect their time consistency and will be discussed later. At this stage we make no modifications to the buoy time series.

#### 2.1.4. Double-Frequency Microseisms

Here we use band-passed data at periods 3 to 13.5 s from the vertical components of seismometers. This frequency band is generally dominated by seismic Rayleigh waves that are generated by opposing waves with periods twice as large, that is, 6 to 27 s (Longuet-Higgins, 1950; Hasselmann, 1963; Ardhuin et al., 2011). Previous authors have analyzed trends and variability of microseism power (Bernard, 1990; Grevemeyer et al., 2000; Aster et al., 2008; Stutzmann et al., 2012) and discussed its relation to the wave climate variability. For some seismic stations, it is possible to estimate neighboring wave heights from the seismic record (Zopf et al., 1976; Bromirski et al., 1999), but this is not possible everywhere because some seismic station are sensitive to waves located as far as 2,000 km away or more (Vinnik, 1973; Ardhuin et al., 2011; Stutzmann et al., 2012). Different type of wave events give different relations between wave and seismic amplitudes (Ardhuin et al., 2012; Obrebski et al., 2012). For example, off the California coast, the relation between the seismic and ocean wave PSDs (power spectral densities) is nearly linear in summer and quadratic in winter. Instead, we simulate the microseism spectra, following Ardhuin et al. (2011) and Stutzmann et al. (2012), and compare the trends in modeled and observed microseisms. This projection of the model onto the observation space has the advantage of taking into account the complex effect of ocean wave directionality. However, it assumes that this directionality is well reproduced by the model, which is generally the case for the wave periods longer than 6 s that we use here (Ardhuin et al., 2013; Peureux & Ardhuin, 2016).

We use eight seismic stations in this work, with locations shown in Figure 3b. All stations are equipped with Streickeisen STS-1 broadband seismometers (Wielandt & Streckeisen, 1982). Three stations are located in Western Europe and are mostly sensitive to waves in the North Atlantic: (1) station GRA1 of the Gräfenberg array in Germany (Harjes & Seidl, 1978); (2) Eskdalemuir, in Scotland (ESK); and (3) Saint Sauveur, in France (SSB), from the Geoscope network (Romanowicz et al., 1984; Stutzmann et al., 2012). The other stations are also from the Geoscope Network: (4) Kipapa, Hawaii (KIP); (5) station near Canberra in Australia (CAN); (6) Crozet Island (CRZ); (7) Inuyama in Japan (INU); and (8) Papeete in French Polynesia (PPT).

Our numerical modeling of the seismic spectrum uses the equivalent long-wavelength pressure spectra $F_{p,2}$ estimated from two wave model simulations. The first simulation uses no reflection. The second model simulation follows Ardhuin et al. (2011) and uses a shoreline reflection parameterized as a function of the shoreface slope, which is estimated (Ardhuin & Roland, 2012) to be twice the slope adjacent to land in the ETOPO2 bathymetry (National Geophysical Data Center, 2006). This may not be the most accurate model (see also Stutzmann et al., 2012), but variations in the treatment of reflection had little impact on the trends

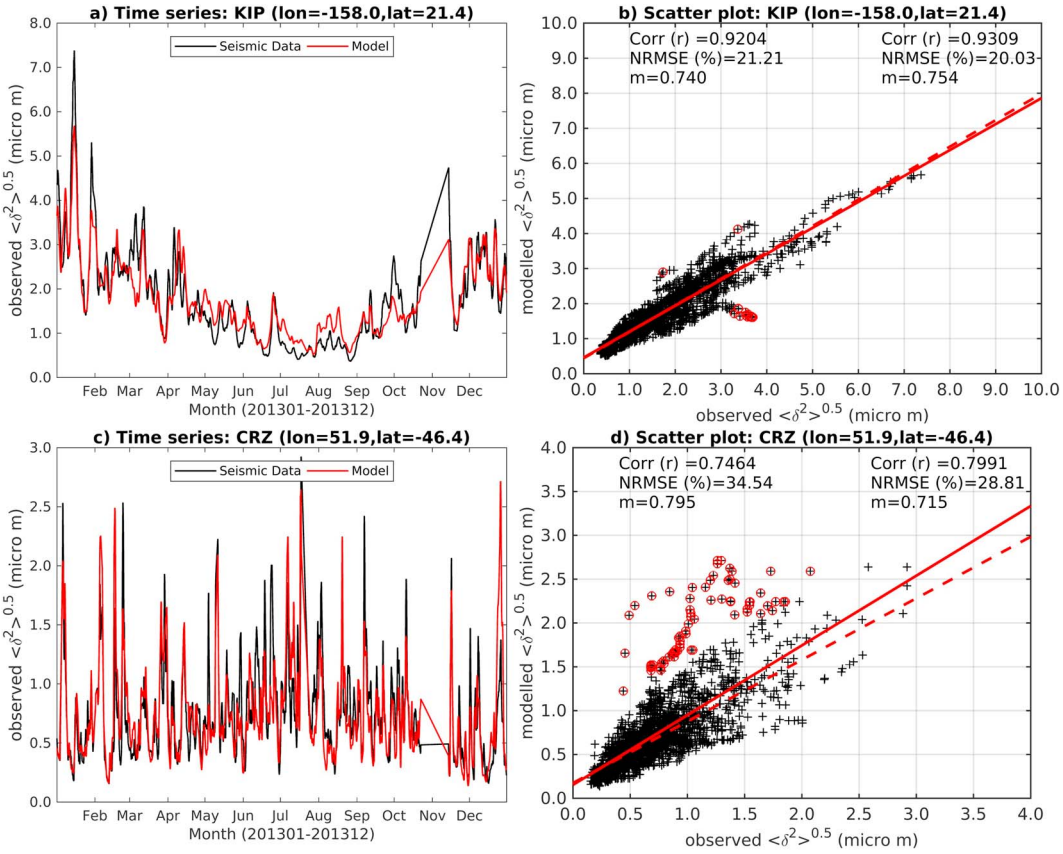


**Figure 4.** Time series for seismic displacement at KIP (a) and CRZ (c) with model estimates. The scatter plots show the comparison for KIP (b) and CRZ (d). The solid red line is the least squared fit and dashed line is the least square fit after outliers are removed. The statistics in panels (b) and (d) show the correlation coefficients (Corr), normalized root mean square error (NRMSE), and slope of the line (m) for all data (left) and after outliers are removed (right).

in general. Furthermore, shoreline reflection can be neglected for the dominant microseisms at stations KIP, CRZ, and PPT, although it is always important for the longest wave periods.

The seismic sources for Rayleigh waves are computed from the $F_{p,2}$ field and summed incoherently over great-circle paths using a constant attenuation factor $Q$. We determine the best $Q$ for each seismic station by minimizing the errors and maximizing the correlation coefficients between the seismic PSD and the wave model data from WW3 for the year of 2013. We find $Q = 110$ for CAN, $Q = 250$ for CRZ, $Q = 180$ for ESK, $Q = 220$ for GRA, $Q = 100$ for INU, $Q = 700$ for KIP, $Q = 610$ for PPT, and $Q = 230$ for SSB. These $Q$ values are consistent with those obtained for the GEOSCOPE stations CAN, INU, PPT, and SSB for the year 2008 by Stutzmann et al. (2012). The higher $Q$ value for KIP station gives a larger contribution to remote sources compared to stations with a lower $Q$: KIP is a good indicator of the wave activity across the entire North Pacific (Ardhuin et al., 2011, their Figure 11).

For the microseisms we consider a frequency interval from 0.076 to 0.312 Hz over which we integrated the vertical ground displacement PSD. This frequency band corresponds to wave periods of 6 to 27 s because the seismic frequency is twice the ocean wave frequency (Longuet-Higgins, 1950). Because we only consider seismic propagation in a spherically symmetric Earth model and neglect 3-D propagation effects, it is difficult to estimate the exact magnitude with the wave model so we scale the model results by the ratio of the average values (mean[seismic]/mean[model]).

We assess the ability of the model to capture the seismic data in Figure 4. In general, the model matches both the annual cycle and the microseismic events that span a few days. At KIP, the correspondence between model and observations is particularly good, thanks to the large-scale integration across much of the North Pacific, which also explains the typically longer duration of microseismic events. The correlation is 0.92 and the normalized root mean square error is 21%. The majority of the significant events are captured by the

model (Figure 4a). The solid red line in Figure 4b represents a least square linear fit between the observations and the model. The linear regression is often sensitive to outliers so we remove outliers by using a bisquare weight function

$$w = (|r| < 1)\left(1 - r^2\right)^2 \tag{1}$$

where

$$r = \frac{\text{res}}{4.685(\text{MAD} \quad /0.6745)\sqrt{1-h}} \tag{2}$$

res is the residual (res = seismic − model), MAD = median(res − median(res)) is the median absolute deviation of the residuals, the constant 0.6745 makes the estimate unbiased for the normal distribution, and the constant 4.685 specifies the weight. We then use the weights to recompute the slope of the least square linear regression to reduce the impact of the outliers. The dashed red lines in Figure 4 represents the linear fit after the reduction of the outliers. The red points show the lowest 5% of the weights. For KIP, the weighting has minimal impact of the slope. At the CRZ station in the Southern Ocean, the model performance is not as good as KIP. Yet the model and observations are still moderately correlated (0.75–0.80). Notice that the Southern Ocean is more active throughout the year with storms (the spikes) occurring throughout the year while the KIP has a stronger seasonality.

### 2.2. Model Implementation

We use version 5.16 of the spectral wave model WAVEWATCH III, hereinafter WW3 (The WAVEWATCH III Development Group, 2016). WW3 solves the action balance equation. This means waves propagating in physical space and spectral space are balanced by the nonconservative source and sink terms. In this study, we use the parameterizations of wave generation and dissipation proposed by Ardhuin et al. (2010) as updated by Rascle and Ardhuin (2013), and the nonlinear Discrete Interaction Approximation by Hasselmann and Hasselmann (1985). This model configuration performs well for $H_s$, higher moments of the wave spectra such as Stokes drift and mean-squared slopes, and swell components compared to other available parameterizations (Stopa et al., 2016). Even though there has been advancements in the physical parameterizations for wave-ice interactions, we do not implement these source terms (e.g., Rogers et al., 2016; Boutin et al., 2018).

We use a global model grid of 0.5° in longitude and latitude with a spectral grid composed of 24 directions and 32 frequencies exponentially spaced from 0.037 to 0.7 Hz at an increment of 10%. All model simulations are forced by CFSR winds. From Figures 1a and 1c it is clear that the $U_{10}$ is often weaker than ALT. However, by changing the wind to wave growth term (called $\beta_{MAX}$) based on the original formulation by Janssen (1991) and adapted by Ardhuin et al. (2010) the errors in the hindcast can be reduced (Stopa, 2018). In the original wave hindcast shown in Figures 1b and 1d we used $\beta_{MAX} = 1.30$, which is close to the calibrated value of 1.385 found for 2001 (Stopa, 2018). The 1-Hz altimeter measurements of $H_s$ are noisy, and we thus smooth the altimeter tracks by taking a running mean for each satellite track using the same spatial scale (5–7 points) as the computational grid (0.5° of 55 km). The model data are then interpolated in time and space to match the altimeter observations.

## 3. Proposed Correction to Wind Speeds

### 3.1. Background

Returning back to Figure 1, we see that the CFSR wind speed is overestimated relative to the altimeter data before 1993 in the Northern (NH: 30°N, 60°N) and Southern (SH: 60°S, 30°S) Hemispheres at P95 (Figure 1c). The NH and SH regions have the highest occurrence of wind seas in the global ocean but they can be dominated by swell (Fan et al., 2014; Semedo et al., 2011). Despite the dominance of swell, we see that the $H_s$ is overestimated corresponding to the U10 overestimation before 1993 in the NH and SH at P50 and P95 (Figures 1b and 1d). Notice that the $H_s$ residuals in the NH and SH follow the same pattern. In Chawla et al. (2013) the overestimation before 1993 was noted in the SH; however, it was not recognized as an issue in the NH. Here we find that there is also an overestimation of $U_{10}$ and $H_s$ in the NH as well but to a lesser extent than the SH. There are several other notable features in the $H_s$ P50 and P95 residuals such as the anomaly in 1996–1999, the increasing trend from 2004 to 2010, and the underestimation of December 2010 right at the transition between v1 and v2 of CFSR. These features are also seen in the $U_{10}$ P95 residuals

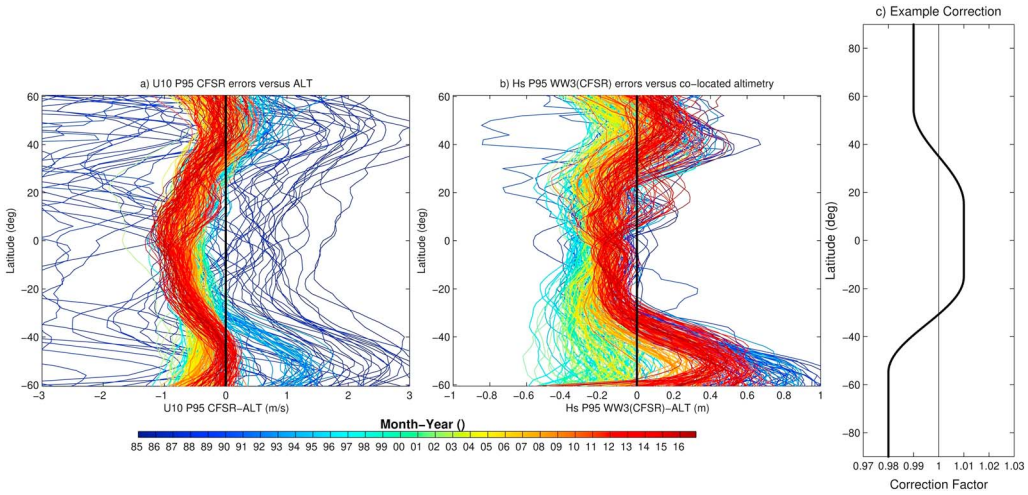


**Figure 5.** The 95th percentile differences between CFSR and ALT as a function of latitude in 1° bins for U10 (a) and $H_s$ (b). Panel (c) shows an example correction as function on latitude used to counteract typical errors seen in (a) and (b). CFSR = Climate Forecast System Reanalysis.

(Figure 3c). It is interesting that the $U_{10}$ P50 residuals do not follow the same pattern as the $U_{10}$ P95, $H_s$ P50, and $H_s$ P95 residuals. For example, the $U_{10}$ P50 residuals begin to decrease after 2010 while the others are relatively stable through this period (2010–2016).

The CFSR $U_{10}$ P95 is slightly underestimated from the period 2010–2016; however, the hindcast $H_s$ P95 is overestimated. A overall mismatch between U10 and $H_s$ can be corrected by reducing $\beta_{MAX}$ (e.g., Stopa, 2018); however, we keep the reference hindcast with $\beta_{MAX} = 1.3$. The $U_{10}$ P95 residuals are typically small (<0.6 m/s). This subtle difference in $U_{10}$ over large areas for the strongest wind speeds will result in larger seas. On average $U_{10}$ P95 in the NH (SH) is 15.5 (16.7) m/s and the $U_{10}$ residual is 0.25 (0.40) m/s; thus, the $U_{10}$ average residual is 1.6 (2.4)%. The $H_s$ P95 in the NH (SH) is 5.1 (6.2) m and the $H_s$ residual is 0.12 (0.32) m; thus, the average $H_s$ residual is 2.4 (5.2)%. In both the NH and SH, the $H_s$ residuals in a percentage are nearly double compared to the $U_{10}$ residuals. This illustrates that the resulting wave field is sensitive to errors in the high wind speeds namely in the extratropics (e.g., NH and SH). In the low latitudes (<25°N/S), swells typically dominant the sea state (Semedo et al., 2011), so a correlation between $U_{10}$ and $H_s$ is weaker (Stopa et al., 2013, Figure 8). To understand interannual climate variability, the consistency of the residuals (or lack of) and trends in Figure 1 is important and not the absolute value (i.e., under/over estimation).

To further explore the errors as function of latitude, we compute the $U_{10}$ and $H_s$ residuals for all latitudes in Figure 5. Here we include the $U_{10}$ from GEOSAT to demonstrate that the data are unreliable. It is common for CFSR to underestimate $U_{10}$ in the tropics 25°N/S compared to the extratropics (>25°N/S). In the SH, from 1992–1994 it is clear the reanalysis is overestimating $U_{10}$. The P95 $H_s$ residuals in Figure 5b show similar features. Note the $H_s$ from GEOSAT are reliable and similar to the hindcast. Similar to the $U_{10}$ residuals, the hindcast overestimates $H_s$ 1985–1993. In addition, the hindcast underestimates the years 2000–2006 especially in the SH. The $H_s$ residuals are relatively larger in the NH and SH compared to the tropics. Also notice that near 60°S the hindcast has a large range of residuals spanning 1.5 m. Previous studies such as Ardhuin et al. (2010) and Stopa et al. (2016) show that $H_s$ residuals between altimeters and spectral wave models are often largest near the ice edge in the Southern Ocean. Therefore, we expect some of the variability here are potentially due to errors of the ice edge location and wave-ice interactions not considered.

### 3.2. Proposed Correction

In this work we make the assumption that the homogeneity of the merged altimeter database is of sufficient quality to correct the a hindcast and in our case CFSR. In Figure 2, especially in 1990s, there are potentially some homogeneity issues between platforms; however, this is out of the scope of this study and interplatform differences are currently being addressed in the SeaStateCCI project. We propose that modifying the wind speed by small percentages can correct errors in the wave field particularly in the North and South Hemispheres (e.g., Figures 1 and 5). To correct for the residuals observed in Figure 5, we propose the following

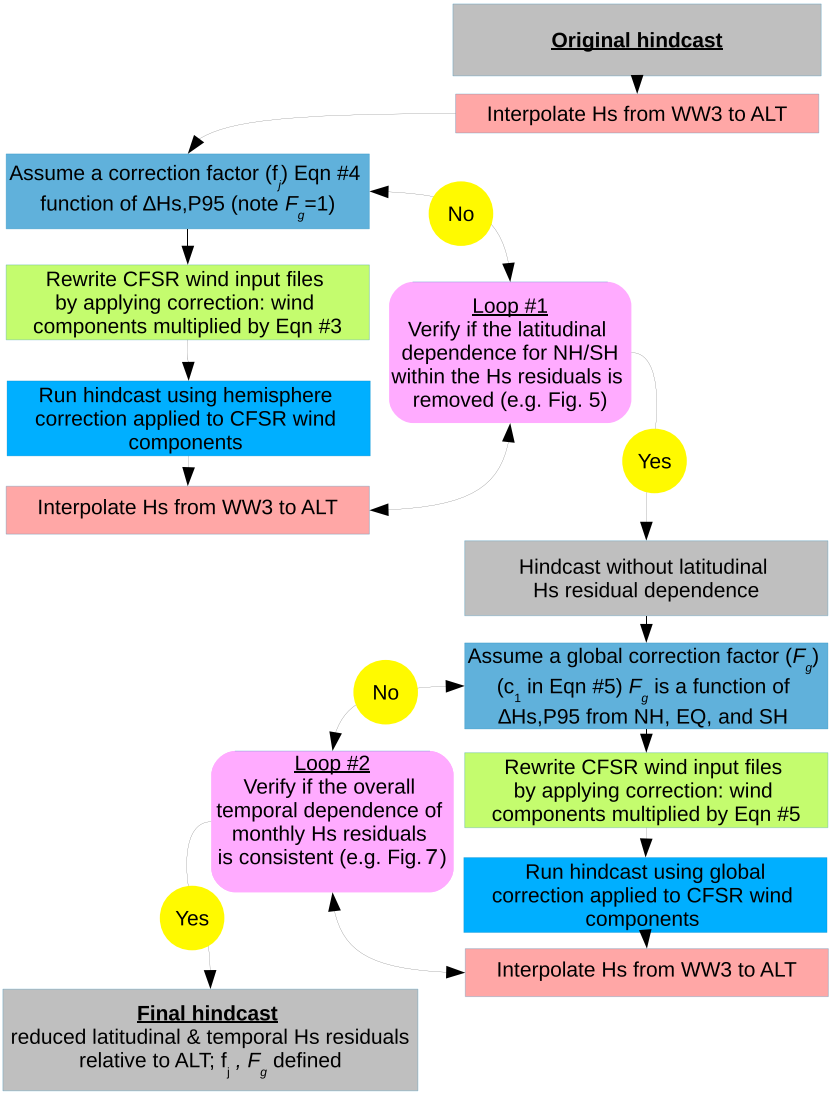


**Figure 6.** Work flow of proposed method to modify reanalysis winds based on $H_s$ residuals. CFSR = Climate Forecast System Reanalysis.

correction as a function of latitude $y_i$ ($\in (-90°,90°)$):

$$C(y_i) = \begin{cases} F_g & \text{for } y_i < |15°| \\ F_g + F_j \left[\frac{1}{2}(1 - \cos\left(\frac{\pi}{N-1}(i-I)\right)\right] & \text{for } 15°| \le y_i \le |55°| \\ F_g + F_j & \text{for } y_i > 55° \end{cases} \quad (3)$$

where $F_g$ is a global correction factor, $F_j$ is the hemisphere correction factor where $j$ is an index representing the NH or SH, $i$ is a latitude index, $I$ is the index where $y_i$ is equal to 15°, and $N$ is the number of latitudes between 15° and 55°. We show our methodology to determine the coefficients $F_j$ and $F_g$ in Figure 6. The basic workflow is composed of two iteration loops to first reduce the latitudinal $H_s$ residuals (WW3-ALT; i.e., find $F_j$) and then reduce the temporal residuals (i.e., find $F_g$).

We provide an example correction of equation (3), which is a function of latitude in Figure 5c. Here the correction ($F_1 = 0.98; F_2 = 0.97; F_g = 1.01$) is a gradual transition from the tropics through the extratropics described by a half-Hanning function. For both the NH and SH ($F_j$), the correction is a function of the $H_s$ monthly difference between the hindcast and ALT at P95 computed over the entirety of the regions (NH:

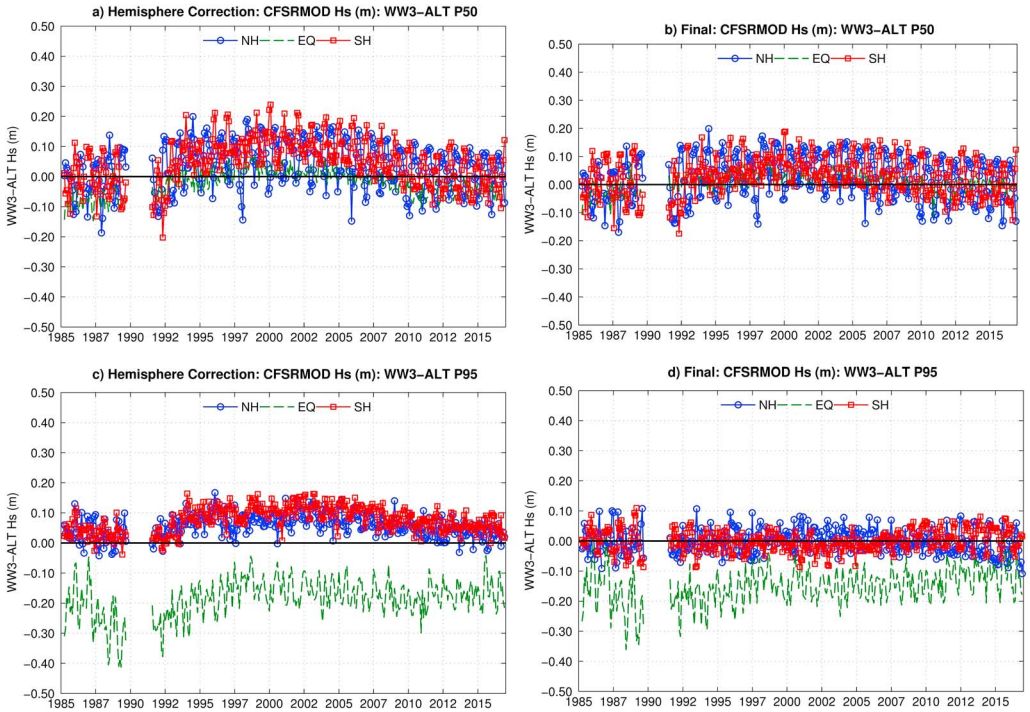


**Figure 7.** Monthly residuals: difference between wave hindcast using CFSR versus altimeter significant wave heights. Northern Hemisphere (NH: 30–60°N), equatorial region (EQ: 30°S to 30°N), and the Southern Hemisphere (SH: 30–60°S) and given in blue (line with circles), green (dashed), and red (line with squares), respectively. Panels (a) and (c) are the residuals after correcting the Northern and Southern Hemispheres, and panels (b) and (d) are the residuals of the final hindcast. Panels (a) and (b) represent the median (P50), and panels (c) and (d) are the 95th percentile (P95). CFSR = Climate Forecast System Reanalysis.

30–60°N and SH: 30–60°S; $\Delta H_{s,P95} = H_{s,P95,WW3} - H_{s,P95,ALT}$)

$$F_j = 1 - \frac{\Delta H_{s,P95}}{f_j \sqrt{2}} \tag{4}$$

where $f_j$ is a calibration factor: $f_{1,NH} = 9.8$ and $f_{2,NH} = 7.6$. Equation (3) is multiplied by east-west ($u$) and north-south ($v$) components of the wind speed.

Following the work flow in Figure 6, we first find the NH and SH corrections (find $F_j$ where initially $F_g = 1$) through iterative wave hindcast generation (loop 1). The $H_s$ residuals after loop 1 in Figure 6 are plotted in Figures 7a and 7c. Comparing these results to Figure 1, it is clear that the time consistency improves. Now the $H_s$ residuals are within ± 0.1 m of ALT instead of ±0.4–0.8 m as in the initial hindcast. The other notable feature is that after the initial correction (loop 1) all regions (NH, EQ, and SH) follow the same pattern for both P50 and P95. We see that the hindcast is stable from 1985 to 1993, increases from 1994 to 1997, stays relatively stable from 1998 to 2004, decreases from 2005 to 2010, and then remains relatively stable from 2010–2016. Therefore, we added an additional "global correction" (loop 2 in Figure 6) by defining $F_g$ as a function of these residuals:

$$F_g = c_1 \times (\overline{\Delta H_{s,P95}}) + c_2 \tag{5}$$

where $c_1$ and $c_2$ are calibration constants that are found through iteration, $\overline{\Delta H_{s,P95}}$ is the unweighted average of the normalized $H_s$ P95 residuals for the NH (30–60°N), EQ (30°S to 30°N), and SH (30–60°S). The final values for $c_1$ and $c_2$ in equation (5) are 0.018 and 0.015, respectively. The normalization is computed by first subtracting the minimum and then dividing by the maximum so the monthly residual time series ranges from 0 to 1. In the EQ (Figure 7c), the wave hindcast after loop 1 underestimates $H_s$ by 0.2 m. To counteract some of the underestimation, we added the factor of $c_2$=0.015. We correspondingly adjusted equation (4)

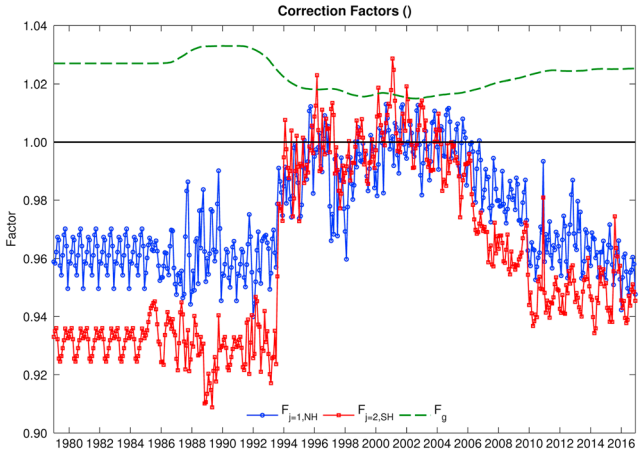


**Figure 8.** Monthly correction factors for the Northern Hemisphere, Southern Hemisphere, and a global factor in blue (solid line with circles; equation (4)), red (solid line with squares; equation (4)), and green (dashed line; equation 5), respectively. The corrections are based on $H_s$ P95 residuals and applied to east-west and north-south wind components.

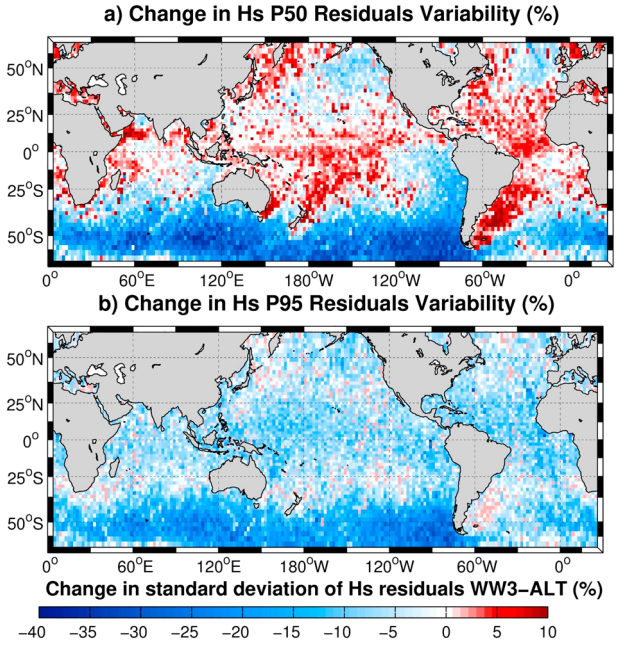


**Figure 9.** Percentage change in the $H_s$ residuals (WW3-ALT) before and after modification to the wind speeds for P50 (a) and P95 (b) on a monthly time series in 2° bins.

by the same $c_2$ factor ($F_{j,(new)} = F_{j,(equation4)} - c_2$). The final hindcast is then associated with all coefficients, which are defined in equations (3)–(5) and applied to the CFSR wind components.

The final correction factors are given in Figure 8 and the final latitudinal corrections are given in Figures 7b and 7d. The global correction counteracts the effects seen in Figures 7a and 7c. The seasonality of the residuals in the NH is typically larger than in the SH, and we see the corrections follow the same pattern. The large discontinuity that occurs in 1994 is the most dramatic feature in Figure 8. Otherwise the same features with opposite sign are seen compared to the initial analysis shown in Figure 1. For the periods when satellite altimetry is not available (1979–1985 and 1990–1991), we applied an average seasonal correction computed from the $H_s$ P95 residuals over the entire period for both the NH and SH. We used an average of 1985–1989 and 1992–1993 for the data gaps in the NH (0.96) and SH (0.93). These assumptions are later assessed when we compare the modified hindcast with the independent buoy and seismic data. The comparison of the final hindcast including both the hemisphere and global corrections is shown in Figures 7b and 7d. By adding the global correction, we are able to take out some of the features seen in Figures 7a and 7c. For the $H_s$ P50 residuals (Figure 7b) some of the same features are seen, but they are reduced compared to Figure 7a. For the $H_s$ P95 residuals there is nearly no trend relative to the altimeters.

The variability of the $H_s$ residuals certainly reduces from the initial hindcast in Figures 1b and 1d compared to the modified hindcast in Figures 7b and 7d. To get an idea of the spatial distribution of change in variability, we calculate the standard deviation of the residuals for a given statistical quantity ($v$) as

$$\sigma_v = \sqrt{\frac{\sum_{k=1}^{M}\left((v_{k,WW3} - v_{k,ALT}) - \overline{(v_{k,WW3} - v_{k,ALT})}\right)^2}{M-1}} \quad (6)$$

where $k$ is a monthly index and $M$ is the total number of months. The change in variability of the residuals is given

$$\Delta\sigma = \frac{\sigma_{v,MOD} - \sigma_{v,ORG}}{\sigma_{v,ORG}} \times 100 \quad (7)$$

where *ORG* is the original wave hindcast and *MOD* represents the modified hindcast after the CFSR wind speeds are changed. This metric is computed for the P50 and P95 and plotted in Figure 9 in a percentage relative to the standard deviation of the original wave hindcast. For the $H_s$ P50 residuals there is clear reduction in the variability in the Southern Ocean of at least 30%. Other regions in the lower latitudes increase in variability on the order of 5%. On the Eastern shore of South America, there is a maximum of nearly 10% increase in the residual variability. For the $H_s$ P95 residuals, there is a reduction of the variability nearly across the entire ocean except a few scattered points that were all less than 2%. The strongest reduction occurs in the Southern Ocean of approximately 20–30%. Therefore, we expect the modified hindcast more closely matches the altimeter database.

## 4. Independent Verification With Buoys and Seismic Data

Next we compare the modified hindcast with buoys and seismic data. We compare the monthly percentiles from the buoys grouped in the eight

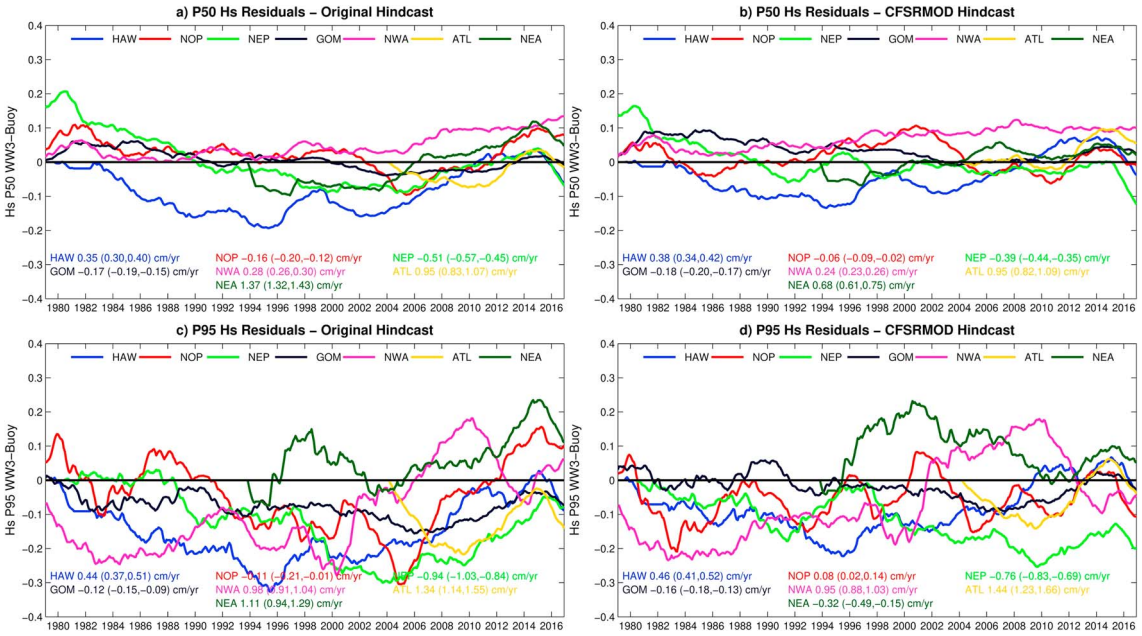


**Figure 10.** Monthly $H_s$ residuals for P50 (a, b) and P95 (c, d) for the original CFSR-forced hindcast and after the hindcast forced by CFSR wind speeds after they were modified (CFSRMOD) at selected buoys grouped into various geographic regions: HAW (Hawaii), NOP (North Pacific), NEP (Northeast Pacific), GOM (Gulf of Mexico), NWA (Northwest Atlantic), ATL (Atlantic), and NEA (Northeast Atlantic). The slope of the linear regression of the residuals between the CFSR hindcasts and ALT is given for each region where the 95% confidence limit is given in the parentheses. CFSR = Climate Forecast System Reanalysis.

regions shown in Figure 3. The time series of the $H_s$ residuals before and after the modification are shown in Figure 10. The seasonal variation of the $H_s$ residuals was strongly observed for the P50 and P95; therefore, we took a running mean of 13 points to suppress this effect. The P50 residuals before and after the modification are similar with only subtle differences in the homogeneity of the time series after modification. Near Hawaii, the negative bias is reduced after modification. In general, the $H_s$ residuals are less than ±0.2 m. The least squared linear regions slopes in Figure 10 show there are only a few regions with statistically significant results namely NOP, NWA, and NEP where the modified CFSR hindcast only slightly reduces the slope of the P50 residuals (meaning more homogeneous). When the confidence limits of the slope do not overlap, the results are considered statistically significant at the 95% limit. The $H_s$ P95 residuals have more variability than $H_s$ P50 residuals. The modified hindcast has $H_s$ P95 residuals closer to zero somewhat improving the accuracy. Otherwise before and after the modification the slopes of the P95 residuals are nearly the same and they are not statistically significant at the 95% confidence limit. The same features are seen before and after the correction with only subtle improvement in the homogeneity of the residual time series for the modified hindcast. For example, in the Northeast Pacific (NEP) after the correction, the negative residuals from 2000 to 2004 reduce. In other regions such as the Northeast Atlantic (NEA), the modified hindcast has positive residuals from 1996 to 2004 that increase. This suggests the hemispheric-wide correction to the reanalysis might not be appropriate for the Pacific and Atlantic. Note that our correction from 1979–1984 and 1990–1991 where we lack $H_s$ from altimetry seem to be adequate because we do not see drastic differences compared to the time periods with altimeters in operation.

We also computed the trend of the residuals to give an indication of the homogeneity of the hindcasts at each buoy. Ideally, there should be no trend in the hindcast-buoy residuals. All buoys were individually analyzed and the median trend (Sen's slope) computed for all months are plotted in Figure 11. The statistical significance is estimated using the Mann Kendall seasonal test (e.g., Young et al., 2011; Stopa & Cheung, 2014b). For $H_s$ P50 and P95 residuals (Figures 10a and 10c), there is often a positive trend in the Northeast Pacific and Hawaii while the buoys near the West Coast of the United States have both increasing and decreasing trends. In the Gulf Mexico and Northwest Atlantic, the trends are also mixed while the buoys in the Atlantic and Northeast Atlantic have increasing trends. After the $U_{10}$ modification, the trend of $H_s$ residuals mostly reduce. This change is most clear in the North Pacific and the $H_s$ residual trends typically reduce by 0.5 cm/year. Improvements are also seen in the Northwest Atlantic with an improvement after the

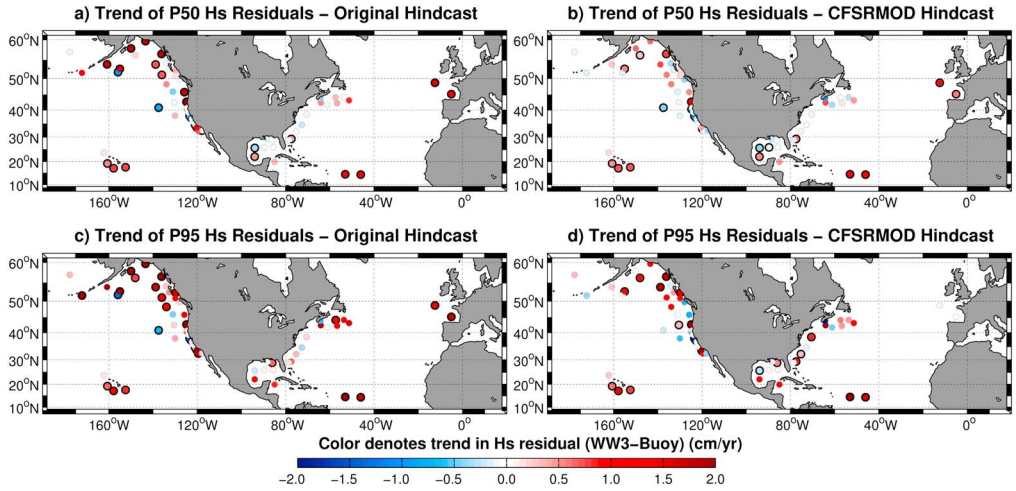


**Figure 11.** Sen's slope computed on monthly $H_s$ residuals for P50 (a, b) and P95 (c, d) for the original CFSR-forced hindcast and after the hindcast forced by CFSR wind speeds after they were modified (CFSRMOD). Statistical significance at the 95th percentile are denoted by the dark black circle. CFSR = Climate Forecast System Reanalysis.

modification. At some select buoys, such as NDBC 44004 (70°W, 38.5°N), the trend of the $H_s$ P95 residuals increases after the modification (Figures 10c and 10d). Very minimal changes are seen near Hawaii before and after modification. In the Northeast Atlantic the trends of the $H_s$ reduce considerably (1 cm/year) after the modification. For each buoy, we calculate the 95% confidence interval of the slope of the $H_s$ residuals. When the confidence intervals overlap the results are considered to be not statistically significant. When the confidence intervals of the slope of the $H_s$ residuals for the original and modified hindcast does not overlap and the trend reduces, we expect that the homogeneity of CFSRMOD improves. Of these 68 buoys, the trend of the residuals reduced at 36 buoys (53%) at the 95 confidence interval. At nine buoys (13%), the trend of the $H_s$ residuals increased after the modification at the 95 confidence interval. This leaves 23 buoys (33%) where trends were not statistically significant. Here we are assuming that the time series of the buoys are consistent; however, previous works show there are issues with the buoy homogeneity (e.g., Aarnes et al., 2015; Gemmrich et al., 2011).

Next we compare the seismic observations to the model results. It is rather difficult to estimate the magnitude of the seismic energy. Similar to Stutzmann et al. (2012) we use two model runs. The first assumes no reflection and the second run which uses a parameterization of shoreline reflection that is probably not optimal (Ardhuin et al., 2011). We use the slope of a least squares linear regression between the seismic observations and model with reduction of the outliers (e.g., Figures 4b and 4d) as an indicator of the hindcast consistency.

We compute a slope for each month for the eight seismic stations for the original and modified CFSR hindcast. The results are shown in Figures 12 and 13. Similar to the $H_s$ residual time series plots, the linear slopes have a distinct seasonality, with larger slopes during the local winter. For the locations in the NH (Figures 12a–12d and 12c), the slopes of the linear regression are less than 1 with correlation coefficients typically of 0.3–0.5 (not shown) in the June-July-August. In the December-January-February, the agreement is usually larger than 1 and have correlation coefficients of 0.8–1 (not shown). This large seasonality is possibly related to a seasonal shift from wind seas (for which shoreline reflection is negligible) to swells for which, except at KIP, reflection becomes more important.

We quantify the consistency of the hindcasts by computing a linear regression of the monthly slope time series. In the NH, at stations GRA1, SSB, KIP (Figure 12), and INU (Figure 12) the modified hindcast has a reduced trend in the monthly slopes indicating that the corrected wind is more homogeneous than the original winds when transformed into seismic displacement. The exception is ESK, where modeled microseism trend slightly increases. At GRA1, SSB (Figure 12), and INU (Figure 12), there was nearly an order of magnitude improvement in the hindcast after the CFSR winds were modified. At all of these locations, the confidence intervals given in the top left corners of each panel before and after modification overlap indicating that the results are not statistically significant at the 95% confidence limit. This is consistent with

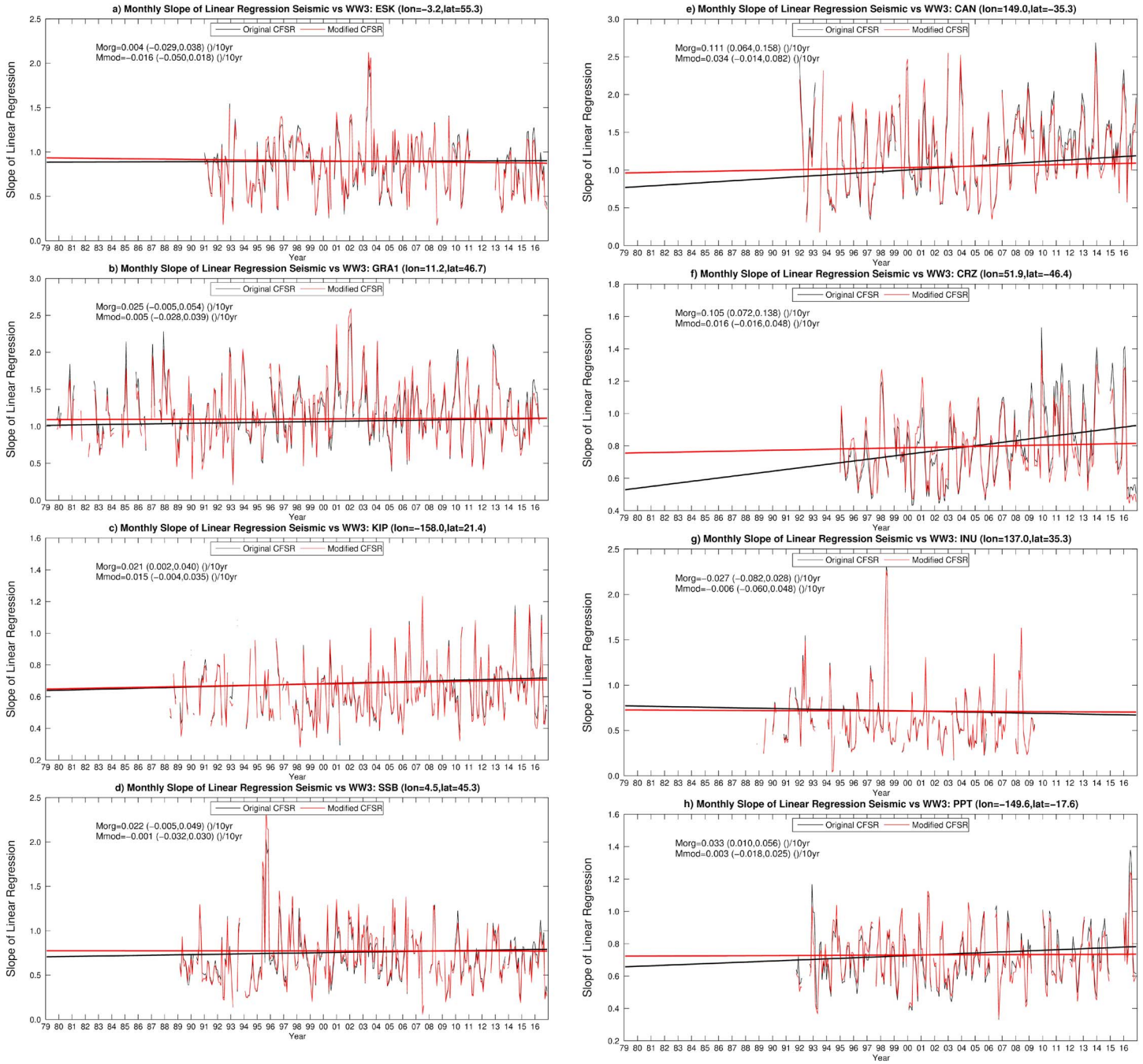


**Figure 12.** Monthly slope of a least squares linear regression between the seismic observations and the model for the ESK (a), GRA1 (b), KIP (c), and SSB (d) from International Federation of Digital Seismograph network-II (a), Global Seismograph Network-IU and Geoscope (c, d) seismic arrays. *Morg* (*Mmod*) is the slope of the linear regression between the seismic observations and the model of the original (modified) CFSR hindcast. Monthly slope of a least squares linear regression between the seismic observations and the model for the CAN (e), CRZ (f), KIP (g), and PPT (h) from the Global Seismograph Network-IU (e–h) seismic arrays. *Morg* (*Mmod*) is the slope of the linear regression between the seismic observations and the model of the original (modified) CFSR hindcast. CFSR = Climate Forecast System Reanalysis.

the fact that there were less changes in the NH compared to the SH shown by the change in $H_s$ residuals (WW3-ALT) in the NH is typically less 10% (e.g., Figure 9). At GRA1, the seismic time series covers the entire period of the hindcast and we see no noticeable change in the 1980s compared to other decades. This suggests that our correction is reasonable for the North Atlantic even when there are no altimeter data.

In Figures 12a, 12b, and 12d we show the corresponding plots for seismic stations in the SH. At CAN, the original hindcast has a relatively large trend in monthly slopes of 0.1 per decade and the modified hindcast greatly improves the homogeneity by reducing the trend by an order of magnitude. At CRZ, the modified hindcast shows a similar improvement in the consistency of the monthly slopes. In this case the change is statistically significant at the 95% limit. At PPT, the modified hindcast improves the homogeneity as well. The confidence intervals of monthly slope time series for the modified hindcast contain zero at all seismic stations. This is not the case for the original hindcast and several stations had trends that were statistically significant different from zero (KIP, CAN, CRZ, and PPT). This indicates that the modified hindcast improves consistency in time. The results indicate that the proposed correction derived from altimeters agrees with seismic stations, a completely independent data source.

## 5. Discussion

In this work, we used data sets from satellites, buoys, and seismic stations to independently assess and correct a wave hindcast. Our intention was not to validate a wave hindcast since many previous studies have done so using CFSR (e.g., Chawla et al., 2013; Rascle & Ardhuin, 2013; Stopa & Cheung, 2014b; Perez et al., 2017). Instead, our focus is to assess and improve the homogeneity of the wave hindcast through use of the various data sets. Our motivation came from the fact that the changing quality and quantity of the data being assimilated into the reanalysis data sets impacts the homogeneity especially in hindcasts using CFSR (Rascle & Ardhuin, 2013; Stopa & Cheung, 2014b). The reanalysis products incorporate the majority of the available observations into them through assimilation. Thus, the plentiful radiometer- and scatterometer-derived wind speeds such as the cross-calibrated multiplatform product (Atlas et al., 2011) have been incorporated into the reanalysis products deeming them unsuitable for independent verification. Therefore, it was necessary to use the independent data sources: altimeters, buoys, and seismic stations to reference the wave hindcasts.

We placed high confidence on the merged altimeter data set because the various satellite platforms have been cross calibrated. This is expected to reduce any spurious discrepancies between platforms that could be equated to trends (e.g., Young et al., 2017). We found deviations of less than 8% between altimeter platforms (see Figure 2) at the $H_s$ P95 suggesting the statistics over large areas are relatively robust. We systematically modified the wind speed using monthly altimeter $H_s$ residuals over large areas of the ocean: SH (30–60°S) and NH (30–60°N). After the modification to CFSR winds, the $H_s$ residuals reduced considerably; thus our assumption that modifying the wind speeds by small percentages (2–7%) reduces errors in the wave field. Since our correction is based on monthly $H_s$ residuals over large areas, a point-by-point comparison between the modified wave hindcast and the altimeters are still largely independent. Thus, the altimeters could be used to further validate the product. Our approach could be considered an advantage over the assimilate technique used by ERAI which directly scales the wave spectra in the wave model by the observed $H_s$ from the altimeters (e.g., Aarnes et al., 2015).

Throughout this work we mainly presented results from the median and upper percentile (P95). We analyzed other percentiles: P10, P25, P90, and P99. The results here from P50 and P95 generally capture the same features of all the statistics. The same features as those in Figure 1 were seen for all percentiles with the lower percentiles having less pronounced deviations. Extremes wave heights ($H_s$ >10 m) are typically of interest, due to their important engineering applications, but they are difficult to capture in wave hindcasts relative to observations (Stopa, 2018). Since our correction was based on P95, the upper wave heights are very stable throughout the hindcast and even more so than the median (see Figure 7). The P99 residuals (WW3-ALT) are very similar the P95 residuals in Figure 7 (not shown). Therefore, we expect that the modified CFSR hindcast is more suitable for analysis of extremes using techniques such as Menéndez et al. (2008) and Izaguirre et al. (2011) since the modified time series more closely follows the stationary assumption.

An obvious downfall of our method is that we assume the altimeter database is consistent in time. The GlobWAVE product includes cross calibration between platforms, but data inconsistencies may arise due to differences in processing and the use of different waveform retrackers. For this reason, we further assessed

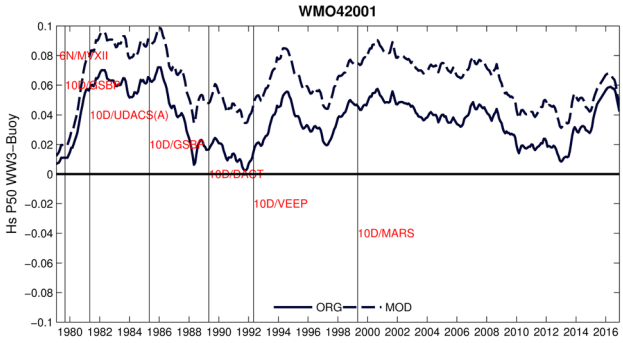


**Figure 13.** Monthly $H_s$ residuals for P50 at buoy 42001 located in the Gulf of Mexico using the hindcasts before (original: *ORG*) and after modification (modified: *MOD*). The vertical lines and red text denote the buoy hull type and wave sensor payload.

the modified hindcast with buoy and seismic data. The comparison with the buoys in the NH from four different networks shows that the homogeneity of the modified hindcast is not drastically different than the original hindcast. At half of the 68 buoys the trend of the $H_s$ residuals reduced after the modification suggesting the correction based on the altimeters improves the time consistency. However, this is complicated by the fact that the buoys are used to correct altimeter biases related to sensor calibration drifts (Queffeulou & Croize-Fillon, 2017). We expect that the minimal change before and after the correction might be because the $H_s$ residuals are caused by inconsistencies in the buoy time series (e.g., Gemmrich et al., 2011). At all of the buoys, the instrument payloads, processing units, and hulls change throughout the 1979–2016 period considered. These changes might be dominating the sometimes large discrepancies seen in Figure 10.

Changes in hulls, sensors, and the processing unit on-board the buoys affect the homogeneity of the $H_s$ time series and when the time series is uncorrected these issues introduce errors in estimating long-term trends (Gemmrich et al., 2011). To further stress this point, we consider NDBC buoy 42001 in the Gulf of Mexico approximately 330 km south of Louisiana (90.0°W, 25.9°N). The buoy was nearly active for the entire hindcast (1979–2016). In Figure 12 we show the changes in hull and sensor payloads. For example, 10*D*/*VEEP* beginning in May 1999 denotes a 10-m discus buoy with the Value Engineered Environmental Payload (VEEP); the metadata describing the changes can be found (http://www.ndbc.noaa.gov/data_availability/data_avail.php). Beyond June 2003 there are no meta data of hull or payload changes noted. In this example, the original and modified wave hindcasts are strongly correlated ($r = 0.98$) with the modified hindcast having a $H_s$ reduced bias of 4 cm throughout the time series. In this case, it is unclear whether the changes in the hull type and sensors impacts the homogeneity, but often strong trends in the residuals are seen during the 1979–1981 (10D/GSBP) and the 1985–1989 (10D/GSBP) time periods. Using significance test of Wang (2008) at the sensor, hull, or processor changes and reducing the impacts of these spurious changes could enable further insights to the wave climate variability or trends over long time series (e.g., Gemmrich et al., 2011). However, the current state of these time series makes it difficult to understand climate variability.

Seismometers measure ground motion created from ocean wave interaction (Longuet-Higgins, 1950; Hasselmann, 1963) and the seismic PSD is expected to represent storminess over large expanses of ocean. Therefore, we expect seismic PSD to be a relatively robust measure of the sea state in time. In the NH, there are mostly small improvements in the consistency of the modified hindcast relative to the seismic observations. This reflects the fact that in the NH we only saw small changes in the $H_s$ variability (e.g., Figure 9) after modification and with respect to the buoys (e.g., Figures 10 and 11). In the SH, there is a clear improvement of the modified hindcast time consistency. Notable changes were seen at CRZ which is located in the "roaring 50s" of the SH and where large inconsistencies of the CFSR hindcast were observed (their Figure 15 Stopa & Cheung, 2014b). There are many well archived and organized global seismic networks such as GEOSCOPE that contain numerous stations for several decades. This manuscript demonstrates the usefulness of these data in validating wave hindcasts. Furthermore, various nondigitized seismic records exist back into the early part of the twentieth century, which could potentially be further exploited to understand climate change.

## 6. Conclusion

In conclusion, we improved the homogeneity of a wave hindcast by use of a multiplatform and calibrated altimeter data set. It was accomplished by empirically scaling wind speeds based on $H_s$ hindcast-altimeter residuals over large zonal regions (NH, EQ, and SH) of the oceans using monthly statistics. In this way, we remove the climatology biases created by changes of the assimilated data in the reanalysis winds. Our method could be applied to correct other wave hindcasts driven by reanalysis data sets. This decision to use the altimeters as a basis was due to the fact that they have global coverage and are expected to have homogeneous record due to the satellite-buoy calibration and cross-platform calibration.

We independently verified the modified hindcast with buoys and seismic stations. We only saw minimal improvement in the consistency between the modified hindcast relative to the buoys located in the Northern Hemisphere. It is difficult to interpret these results because we expect that the buoy time series are influenced by changes in hull, payloads, and processing. The comparison with seismic data show the modified hindcast improves consistency most notably in the Southern Hemisphere. The use of seismic observations is highly advantageous because digital data records exist for several decades and stations are located in the remote undersampled regions namely in the Southern Hemisphere. This demonstrates that the use of seismic observations and our propagation model is an extremely valuable technique to validate wave hindcasts where observations in remote places are scarce, especially since seismic records exist in the early twentieth century and could be digitized (e.g., Grevemeyer et al., 2000). Our results indicate that the altimeters, modified wave hindcast, and seismic stations are in closer agreement throughout the time series. The modified hindcast will be useful for improving our understanding of the wave climate, in particular how the interannual variability and secular trends combine.

**Acknowledgments**
This work is supported by LabexMER via grant ANR-10-LABX-19-01, EU-FP7 project SWARP under grant agreement 607476, ONR grant N0001416WX01117, and the ANR (Agence National de Recherche) project grant ANR-14-CE01-0012. The altimeter data set can be obtained from ftp.ifremer.fr/ifremer/cersat/products/swath/altimeters/waves/ website. The NDBC, CDIP, and MEDS buoy data can be accessed from www.ndbc.noaa.gov website. The OCEANSITES buoy data can be accessed from www.oceansites.org website. The CFSR wind fields and ice concentrations can be obtained from rda.ucar.edu website. The GRA1 and the Geoscope seismic data can be obtained from the FDSN web services at https://eida.bgr.de and http://seismology.resif.fr websites, respectively. The seismic data has been processed using the ObsPy python toolbox (Krischer et al., 2015).

## References

Aarnes, O. J., Abdalla, S., Bidlot, J.-R., & Breivik, Ø. (2015). Marine wind and wave height trends at different ERA-Interim forecast ranges. *Journal of Climate*, *28*(1), 819–837.

Ardhuin, F., Balanche, A., Stutzmann, E., & Obrebski, M. (2012). From seismic noise to ocean wave parameters: General methods and validation. *Journal of Geophysical Research*, *117*, C05002. https://doi.org/10.1029/2011JC007449

Ardhuin, F., Lavanant, T., Obrebski, M., Marié, L., Royer, J.-Y., d'Eu, J.-F., et al. (2013). A numerical model for ocean ultra low frequency noise: Wave-generated acoustic-gravity and Rayleigh modes. *Journal of the Acoustical Society of America*, *134*(4), 3242–3259.

Ardhuin, F., Rogers, E., Babanin, A. V., Filipot, J.-F., Magne, R., Roland, A., et al. (2010). Semiempirical dissipation source functions for ocean waves. Part I: Definition, calibration, and validation. *Journal of Physical Oceanography*, *40*(9), 1917–1941. https://doi.org/10.1175/2010JPO4324.1

Ardhuin, F., & Roland, A. (2012). Coastal wave reflection, directional spread, and seismoacoustic noise sources. *Journal of Geophysical Research*, *117*, C00J20. https://doi.org/10.1029/2011JC007832

Ardhuin, F., Stutzmann, E., Schimmel, M., & Mangeney, A. (2011). Ocean wave sources of seismic noise. *Journal of Geophysical Research*, *116*, C09004. https://doi.org/10.1029/2011JC006952

Aster, R. C., McNamara, D. E., & Bromirski, P. D. (2008). Multidecadal climate-induced variability in microseisms. *Seismological Research Letters*, *79*(2), 194–202.

Atlas, R., Hoffman, R. N., Ardizzone, J., Leidner, S. M., Jusem, J. C., Smith, D. K., & Gombos, D. (2011). A cross-calibrated, multiplatform ocean surface wind velocity product for meteorological and oceanographic applications. *Bulletin of the American Meteorological Society*, *92*(2), 157–174.

Bernard, P. (1990). Historical sketch of microseisms from past to future. *Physics of the Earth and Planetary Interiors*, *63*, 145–150.

Boutin, G., Ardhuin, F., Dumont, D., Sévigny, C., & Girard-Ardhuin, F. (2018). Floe size effects on wave-ice interactions: Theoretical background, implementation and applications. *Journal of Geophysical Research: Oceans*, *123*, 4779–4805. http://doi.org/10.1029/2017JC013622

Bromirski, P. D., Flick, R. E., & Graham, N. (1999). Ocean wave height determined from inland seismometer data: Implications for investigating wave climate changes in the NE Pacific. *Journal of Geophysical Research*, *104*(C9), 20,753–20,766.

Caires, S., & Sterl, A. (2005). A new nonparametric method to correct model data: Application to significant wave height from the ERA-40 re-analysis. *Journal of Atmospheric and Oceanic Technology*, *22*(4), 443–459.

Cavaleri, L., Fox-Kemper, B., & Hemer, M. (2012). Wind waves in the coupled climate system. *Bulletin of the American Meteorological Society*, *78*, 1651–1661.

Chawla, A., Spindler, D. M., & Tolman, H. L. (2013). Validation of a thirty year wave hindcast using the climate forecast system reanalysis winds. *Ocean Modelling*, *70*, 189–206.

Dee, D. P., Uppala, S. M., Simmons, A. J., Berrisford, P., Poli, P., Kobayashi, S., et al. (2011). The ERA-interim reanalysis: Configuration and performance of the data assimilation system. *Quarterly Journal of the Royal Meteorological Society*, *137*(656), 553–597.

Fan, Y., Lin, S.-J., Griffies, S. M., & Hemer, M. A. (2014). Simulated global swell and wind-sea climate and their responses to anthropogenic climate change at the end of the twenty-first century. *Journal of Climate*, *27*(10), 3516–3536.

Fan, Y., Lin, S.-J., Held, I. M., Yu, Z., & Tolman, H. L. (2012). Global ocean surface wave simulation using a coupled atmosphere–wave model. *Journal of Climate*, *25*(18), 6233–6252.

for Medium-Range Weather Forecasts, E. C. (2017). Era5 reanalysis (Tech. rep.) Boulder, Colo.: European Centre for Medium-Range Weather Forecasts through the Research Data Archive at the National Center for Atmospheric Research, Computational and Information Systems Laboratory. (Updated monthly). https://doi.org/10.5065/D6X34W69

Gemmrich, J., Thomas, B., & Bouchard, R. (2011). Observational changes and trends in northeast pacific wave records. *Geophysical Research Letters*, *38*, L22601. https://doi.org/10.1029/2011GL049518

Gourrion, J., Vandemark, D., Bailey, S., Chapron, B., Gommenginger, G. P., Challenor, P. G., & Srokosz, M. A. (2002). A two-parameter wind speed algorithm for ku-band altimeters. *Journal of Atmospheric and Oceanic Technology*, *19*(12), 2030–2048.

Grevemeyer, I., Herber, R., & Essen, H.-H. (2000). Microseismological evidence for a changing wave climate in the northeast Atlantic Ocean. *Nature*, *408*, 349–351.

Harjes, H., & Seidl, D. (1978). Digital recording and analysis of broad-band seismic data at Gräfenberg (GRF) Array. *Journal of Geophysics-Zeitschrift fur Geophysik*, *44*(5), 511–523.

Hasselmann, K. (1963). A statistical analysis of the generation of microseisms. *Reviews of Geophysics*, *1*(2), 177.

Hasselmann, S., & Hasselmann, K. (1985). Computation and parameterizations of the nonlinear energy transfer in a gravity-wave spectrum. Part I: A new method for efficient computations of the exact nonlinear transfer. *Journal of Physical Oceanography*, *15*, 1369–1377.

Hemer, M. A., Zieger, S., Durrant, T., O'Grady, J., Hoeke, R. K., McInnes, K. L., & Rosebrock, U. (2017). A revised assessment of Australia's national wave energy resource. *Renewable Energy*, *114*, 85–107.

Izaguirre, C., Méndez, F. J., Menéndez, M., & Losada, I. J. (2011). Global extreme wave height variability based on satellite data. *Geophysical Research Letters*, *38*, L10607. https://doi.org/10.1029/2011GL047302

Janssen, PeterA. E. M. (1991). Quasi-linear theory of wind-wave generation applied to wave forecasting. *Journal of Physical Oceanography*, *21*(11), 1631–1642.

Kedar, H., Longuet-Higgins, M., Webb, F., Graham, C., Clayton, R., & Jones, C. (2007). The origin of deep ocean microseisms in the north atlantic ocean. *Proceedings of the Royal Society*, *464*, 555–572. https://doi:10.1098/rspa.2007.0277

Krischer, L., Megies, T., Barsch, R., Beyreuther, M., Lecocq, T., Caudron, C., & Wassermann, J. (2015). ObsPy: A bridge for seismology into the scientific Python ecosystem. *Computational Science & Discovery*, *8*(1), 14003. http://iopscience.iop.org/1749-4699/8/1/014003

Longuet-Higgins, M. S. (1950). A theory of the origin of microseisms. *Philosophical Transactions of the Royal Society A: Mathematical, Physical and Engineering Sciences*, *243*(857), 1–35.

Menéndez, M., Méndez, F. J., Losada, I. J., & Graham, N. E. (2008). Variability of extreme wave heights in the northeast pacific ocean based on buoy measurements. *Geophysical Research Letters*, *35*, L22607. https://doi.org/10.1029/2008gl035394

National Geophysical Data Center (2006). Etopo2v2 2-minute global relief model, National Geophysical Data Center, NOAA. https://doi.org/72810.7289/v5j1012q

Obrebski, M., Ardhuin, F., Stutzmann, E., & Schimmel, M. (2012). How moderate sea states can generate loud seismic noise in the deep ocean. *Geophysical Research Letters*, *39*, L11601. https://doi.org/10.1029/2012GL051896

Perez, J., Menendez, M., & Losada, I. J. (2017). GOW2: A global wave hindcast for coastal applications. *Coastal Engineering*, *124*, 1–11.

Peureux, C., & Ardhuin, F. (2016). Ocean bottom pressure records from the cascadia array and short surface gravity waves. *Journal of Geophysical Research: Oceans*, *121*, 2862–2873. https://doi.org/10.1002/2015jc011580

Queffeulou, P. (2013). Merged altimeter wave height data base. An update. In *Proceedings ESA Living Planet Symposium, 2013*, ESA, Nordwijk, The Netherlands, pp. 1–5.

Queffeulou, P., & Croize-Fillon, D. (2017). Global altimeter SWH data set (*11.4*): IFREMER/CERSAT. ftp://ftp.ifremer.fr/ifremer/cersat/products/swath/altimeters/waves/doc\ignorespacesumentation/altimeter_wave_merge_11.4.pdf

Rascle, N., & Ardhuin, F. (2013). A global wave parameter database for geophysical applications. Part 2: Model validation with improved source term parameterization. *Ocean Modelling*, *70*, 174–188. https://doi.org/10.1016/j.ocemod.2012.12.001

Reguero, B., Menéndez, M., Méndez, F. J., Mínguez, R., & Losada, I. (2012). A global ocean wave (GOW) calibrated reanalysis from 1948 onwards. *Coastal Engineering*, *65*, 38–55.

Rogers, W. E., Thomson, J., Shen, H. H., Doble, M. J., Wadhams, P., & Cheng, S. (2016). Dissipation of wind waves by pancake and frazil ice in the autumn Beaufort Sea. *Journal of Geophysical Research: Oceans*, *121*, 7991–8007. https://doi.org/10.1002/2016JC012251

Romanowicz, B., Cara, M., Fel, J. F., & Rouland, D. (1984). Geoscope: A French initiative in long-period three-component global seismic networks. *Eos, Transactions American Geophysical Union*, *65*(42), 753–753.

Saha, S., Moorthi, S., Pan, H.-L., Wu, X., Wang, J., Nadiga, S., et al. (2010). The NCEP Climate Forecast System Reanalysis. *Bulletin of the American Meteorological Society*, *91*(8), 1015–1057. https://doi.org/10.1175/2010BAMS3001.1

Saha, S., Moorthi, S., Wu, X., Wang, J., Nadiga, S., Tripp, P., et al. (2014). The NCEP climate forecast system version 2. *Journal of Climate*, *27*(6), 2185–2208. https://doi.org/10.1175/JCLI-D-12-00823.1

Semedo, A., Sušelj, K., Rutgersson, A., & Sterl, A. (2011). A global view on the wind sea and swell climate and variability from ERA-40. *Journal of Climate*, *24*(5), 1461–1479.

Sepulveda, H. H., Queffeulou, P., & Ardhuin, F. (2015). Assessment of SARAL AltiKa wave height measurements relative to buoy, Jason-2 and Cryosat-2 data. *Marine Geodesy*, *38*(S1), 449–465.

Stopa, J. E. (2018). Wind forcing calibration and wave hindcast comparison using multiple reanalysis and merged satellite wind datasets. *Ocean Modelling*, *127*, 55–69. https://doi.org/10.1016/j.ocemod.2018.04.008

Stopa, J. E., Ardhuin, F., Babanin, A., & Zieger, S. (2016). Comparison and validation of physical wave parameterizations in spectral wave models. *Ocean Modelling*, *103*, 2–17.

Stopa, J. E., & Cheung, K. F. (2014a). Intercomparison of wind and wave data from the ECMWF reanalysis interim and the NCEP Climate Forecast System Reanalysis. *Ocean Modelling*, *75*, 65–83.

Stopa, J. E., & Cheung, K. F. (2014b). Periodicity and patterns of ocean wind and wave climate. *Journal of Geophysical Research: Oceans*, *119*, 5563–5584. https://doi.org/10.1002/2013jc009729

Stopa, J. E., Cheung, K. F., Tolman, H. L., & Chawla, A. (2013). Patterns and cycles in the Climate Forecast System Reanalysis wind and wave data. *Ocean Modelling*, *70*, 207–220. http://doi.org/10.1016/j.ocemod.2012.10.005

Stutzmann, E., Schimmel, M., & Ardhuin, F. (2012). Modeling long-term seismic noise in various environments. *Geophysical Journal International*, *191*, 707–722.

The WAVEWATCH III Development Group (2016). User manual and system documentation of WAVEWATCH III version 5.16 (*329*). College Park, MD, USA: NOAA/NWS/NCEP/MMAB. 326 pp. + Appendices.

Vinnik, L. P. (1973). Sources of microseismic P waves. *Pure and Applied Geophysics*, *103*(1), 282–289.

Wang, X. L. (2008). Accounting for autocorrelation in detecting mean shifts in climate data series using the penalized MaximaltorFTest. *Journal of Applied Meteorology and Climatology*, *47*(9), 2423–2444.

Wang, X. L., & Swail, V. R. (2001). Changes of extreme wave heights in Northern Hemisphere oceans and related atmospheric circulation regimes. *Journal of Climate*, *14*(10), 2204–2221.

Wielandt, E., & Streckeisen, G. (1982). The leaf spring seismometer: Design and performance. *Bulletin of the Seismological Society of America*, *72*, 2349–2367.

Young, I. R., Sanina, E, & Babanin, A. V. (2017). Calibration and cross validation of a global wind and wave database of altimeter, radiometer, and scatterometer measurements. *Journal of Atmospheric and Oceanic Technology*, *34*(6), 1285–1306.

Young, I. R., Zieger, S., & Babanin, A. V. (2011). Global trends in wind speed and wave height. *Science*, *332*(6028), 451–455. https://doi.org/10.1126/science.1197219

Zieger, S., Vinoth, J., & Young, I. R. (2009). Joint calibration of multiplatform altimeter measurements of wind speed and wave height over the past 20 years. *Journal of Atmospheric and Oceanic Technology*, *26*(12), 2549–2564.

Zopf, D. O., Creech, H. C., & Quinn, W. H. (1976). The wavemeter: A land-based system for measuring nearshore ocean waves. *Marine Technology Society Journal*, *10*(4), 19–25.